Real-Time Broadband Chirped-Pulse Φ-OTDR Using Overlap-Save Polyphase FFT Compression

Guanfeng Chen, Bin Du, Baijie Xu, Huajian Zhong, Wenzhao Yang, Cailing Fu,
Yiping Wang, *Senior Member, IEEE*, and Jun He, *Member, IEEE*

***Abstract*—Phase-sensitive optical time-domain reflectometry (Φ-OTDR) has been applied in distributed acoustic sensing (DAS) of many fields, such as deep-sea geological activity monitoring, oil extraction, and intelligent transportation. However, in Φ-OTDR, the continuous acquisition of broadband acoustic/vibration signals with high spatial resolution has always been a challenge. In this article, a real-time chirped-pulse (CP) Φ-OTDR based on overlap-save polyphase fast Fourier transform (OS-PFFT) optical pulse compression is demonstrated for DAS with high spatial resolution and broadband frequency response. In the proposed system, a polyphase-channel parallel approach is employed for interleaved sampling on Rayleigh backscattering (RBS) signal segments with subsequent FFT processing, thus reducing the computational load while improving data throughput. A pulse compression at a high sampling rate of 3.2 GSa/s has been achieved successfully in a field-programmable gate array (FPGA) without clock constraints. A strain resolution of 26.3 $p\varepsilon/\sqrt{Hz}$ and a spatial resolution of 0.9 m were experimentally achieved at a distance of 25 km, and a spatial resolution of 2.5 m was achieved at 70 km. A low-frequency vibration at 0.01 Hz was detected with a signal-to-noise ratio (SNR) of 48 dB, whereas a maximum detectable frequency of 5 kHz was demonstrated. As a result, the proposed real-time DAS scheme has the potential to facilitate DAS applications with requirements for a wide-range frequency response and rapid sensing capabilities.**

***Index Terms*—Distributed acoustic sensing (DAS), field-programmable gate array (FPGA), phase-sensitive optical time-domain reflectometry.**

NOMENCLATURE

$r(\tau)$	Rayleigh backscattering complex reflection coefficient corresponding to the round-trip delay τ.
$x[n]$	Sampled analytic beat-signal sequence.
$h[n]$	Sampled matched-filter kernel.
$y[n]$	Discrete pulse-compressed output sequence.
L_h	Effective length of the sampled matched-filter kernel $h[n]$.
$winL$	FFT block length used in overlap-save processing.
D	Block hop size / valid output length retained from each block.
M	Number of polyphase branches.
P	Number of FFT points per phase, with $winL = MP$.

I. INTRODUCTION

DISTRIBUTED acoustic sensing (DAS) technology is of great significance in various application fields such as oil extraction [1], power cable patrol inspection [2], and intelligent transportation [3], [4], [5]. The phase-sensitive optical time-domain reflectometry (Φ-OTDR), serving as a representative type of DAS technology, functions by launching coherent laser pulses to interrogate optical fibers, and derives the longitudinal strain distribution by extracting the phase of Rayleigh backscattering (RBS) light from the fiber. In most applications, a fundamental challenge involves balancing signal-to-noise ratio (SNR), spatial resolution, and sensing range through systematic tradeoff quantification. For instance, increasing pulsewidth enhances SNR and sensing range while sacrificing the spatial resolution. Furthermore, insufficient demodulation speed in a DAS system forces a tradeoff between reducing the analog-to-digital converter (ADC) sampling frequency and decreasing pulse repetition rate to prevent missed detection events during real-time monitoring. The former limits the modulation bandwidths and sensing performance in a DAS system, while the latter leads to frequency response bandwidth contraction and background noise aliasing into the low-frequency detection band [6], [7]. Therefore, there is an urgent need for a high-performance real-time DAS system that could simultaneously cover ultralow-frequency vibration and conventional acoustic bands.

Recently, several methods have been proposed to achieve high-SNR vibration measurement in the sub-Hz frequency band [8], [9], [10], [11], [12], [13]. Sun et al. [8] implemented a strain-free fiber with a scatter-enhanced points (SEPs) array as a reference, achieving 0.01-Hz detection with 30.4-dB SNR [8]. In the same year, Wang et al. [9] developed a chirped-pulse (CP) Φ-OTDR system employing a random fiber grating array (RFGA) as a sensing element, integrated with

Received 28 January 2026; revised 2 April 2026; accepted 10 April 2026. Date of publication 6 May 2026; date of current version 20 May 2026. This work was supported in part by the National Natural Science Foundation of China under Grant 62435012, Grant U22A2088, and Grant U25B2051; in part by Shenzhen Science and Technology Program under Grant 20241209093330001; and in part by China Postdoctoral Science Foundation under Grant 2024M762125 and Grant 2025M780791. The Associate Editor coordinating the review process was Dr. Enes Ataç. *(Corresponding author: Jun He.)*

The authors are with the State Key Laboratory of Radio Frequency Heterogeneous Integration, Key Laboratory of Optoelectronic Devices and Systems of Ministry of Education/Guangdong Province, College of Physics and Optoelectronic Engineering, Shenzhen University, Shenzhen 518060, China, and also with the Shenzhen Key Laboratory of Photonic Devices and Sensing Systems for Internet of Things, Guangdong and Hong Kong Joint Research Centre for Optical Fibre Sensors, Shenzhen University, Shenzhen 518060, China (e-mail: 2200453041@email.szu.edu.cn; dubin2016@email.szu.edu.cn; xubaijie@szu.edu.cn; zhonghj@szu.edu.cn; 2210452120@email.szu.edu.cn; fucailing@szu.edu.cn; ypwang@szu.edu.cn; hejun07@szu.edu.cn).

Digital Object Identifier 10.1109/TIM.2026.3690821

a reference random fiber grating for laser frequency drift monitoring. This configuration enabled dynamic strain reconstruction in the 0.01–20-Hz range [9]. The RBS-enhanced fiber (SEPs and RFGA) could effectively increase the signal SNR but significantly increases the cost in processing systems. Vidal-Moreno et al. [10] demonstrated that their CP Φ-OTDR system could maintain long-term stability exceeding two months by prebuilding a static reference "database." The assistant algorithm (laser frequency drift monitoring and static reference "database") significantly increased system complexity and time consumption in practical applications due to potential database reconstruction requirements under changing environmental conditions. In addition, in [11], [12], and [13], dynamic phase reference information was obtained via dual-pulse fiber injection, aiding in extracting < 1-Hz perturbation signals from low-frequency noise. Unfortunately, the trade-off between spatial resolution and sensing distance persisted due to the single-frequency narrow pulses. Besides, achieving broadband acoustic wave measurement across both low frequencies and conventional vibration frequencies requires real-time processing of a significantly larger volume of data, which places extremely high demands on the processing performance of the system.

Several methods have been demonstrated to achieve real-time processing of large volumes of RBS data. The first approach involves using a band-sampling technique to reduce the data volume while preserving most critical information [14], [15], [16]. Alternatively, optimizing the quantization bit depth to alleviate data processing load represents an effective strategy [17], [18]. However, band-sampling imposes strict constraints on the modulation pulse bandwidth, which severely limits improvements in spatial resolution. Moreover, small quantization bit widths can lead to significant noise accumulation during the demodulation process, thereby degrading sensing accuracy. The second strategy involves using optical or electronic devices to directly implement the Hilbert transform, thereby reducing the complexity of digital signal processing. For example, in [19], [20], and [21], a 90° optical hybrid is employed for in-phase/quadrature (IQ) demodulation, while electrical IQ mixers [22] or 3-dB quadrature mixers [23] were applied to extract I/Q components. Although these additional devices significantly enhance data processing speed, they increase the system cost and may introduce signal noise overextended operation. In addition, field-programmable gate arrays (FPGAs) and graphics processing units (GPUs) represent suitable hardware choices for accelerating the DAS demodulation process [24], [25], [26], [27], [28]. For instance, Sha et al. [27] utilized a GPU to perform parallel computation on time series data at different spatial locations, significantly enhancing computational speed. He et al. [28] employed three decoding filters in an FPGA and achieved real-time pulse compression and fading noise suppression, achieving a noise floor of approximately −20 dB $\mathrm{n}\varepsilon/\sqrt{\mathrm{Hz}}$ under conditions of 3-m spatial resolution and a 10-kS/s interrogation rate [28]. Beyond these electronic-domain approaches, all-optical and photonic–electronic hybrid FFT processors have also been explored for high-throughput signal processing. All-optical FFT architectures can deliver extremely high data rates but are not well suited for the large transform sizes required in DAS [29]. Hybrid photonic–electronic systems [30] support broader FFT scales, yet their multiply–accumulate operations remain electronic, with photonics mainly serving as parallel I/O. Recent silicon-photonics platforms [31] likewise employ photonic devices primarily for chip-level I/O or fixed linear transforms, while large, reconfigurable FFTs continue to rely on FPGAs or ASICs. These trends indicate that both electronic and photonic–electronic architectures ultimately hinge on efficient digital signal processing organization. The FPGA-based scheme presented in this work offers a practical and effective solution for high-resolution, high-sensitivity, and long-range DAS under streaming DSP constraints. Overlap-save and parallel FFT architectures have been adopted to improve throughput in high-rate implementations [32], [33].

In this work, we present a real-time DAS interrogator system with a broadband frequency response, integrating overlap-save polyphase fast Fourier transform (OS-PFFT) pulse compression into an end-to-end FPGA streaming demodulation pipeline. The OS-PFFT employs an overlap-save algorithm to address the computational load growth with increasing fiber length and a parallel polyphase decomposition strategy to improve FPGA data throughput. This system-level integration translates OS-PFFT into an end-to-end real-time DSP framework, rather than an offline processing block, thereby improving processing efficiency and sensing performance. The system performance, including spatial resolution, sensitivity, and frequency response, was experimentally evaluated, achieving a strain resolution of 26.3 $\mathrm{p}\varepsilon/\sqrt{\mathrm{Hz}}$ at 25 km, with spatial resolution maintained at 0.9 m at 25 km, 1.75 m at 50 km, and 2.5 m at 70 km, and a minimum frequency response of 0.01 Hz while maintaining an interrogation rate of 10 kS/s over a 10-km fiber. Overall, these high-performance metrics render this system suitable for various engineering DAS applications.

II. PRINCIPLE

The CP Φ-OTDR system comprises an interrogator and a sensing fiber, as shown in Fig. 1(a). A linear frequency modulated (LFM) probe light pulse is sent into the optical fiber, and its complex optical field expression is given by [34]

$$E_p(t) = \exp\left[j\left[\omega_c t + \phi(t)\right]\right] E(t) \tag{1}$$

where $E(t) = w(t/T_p)\exp(j2\pi f_0 t + j\pi\kappa t^2)$ is the LFM pulse generated by a direct digital synthesizer (DDS), T_p is the pulse duration, f_0 is the additional frequency induced by the modulator, $w(\bullet)$ is the window function of the LFM pulse, κ is the frequency sweeping rate, ω_c is the central frequency of the laser, and $\phi(t)$ represents that the integral of white Gaussian noise is the phase noise. After passing through the detector, the photocurrent can be expressed as

$$\begin{aligned} i(t) &\\ \propto 2Re &\left\{ \begin{array}{c} \int_0^{T_F} r(\tau)\, w\left(\frac{t-\tau}{T_p}\right) \exp\left[j\left(-\omega_c\tau + \phi(t-\tau) - \phi(t)\right.\right. \\ \left.\left. +\ \pi f_0(t-\tau) + \pi\kappa(t-\tau)^2\right)\right] d\tau \end{array} \right\} \end{aligned} \tag{2}$$

where $r(\tau)$ is the RBS complex reflection coefficient in the fiber corresponding to time delay τ and T_F is the total round-trip time of light in the fiber under test (FUT). After applying

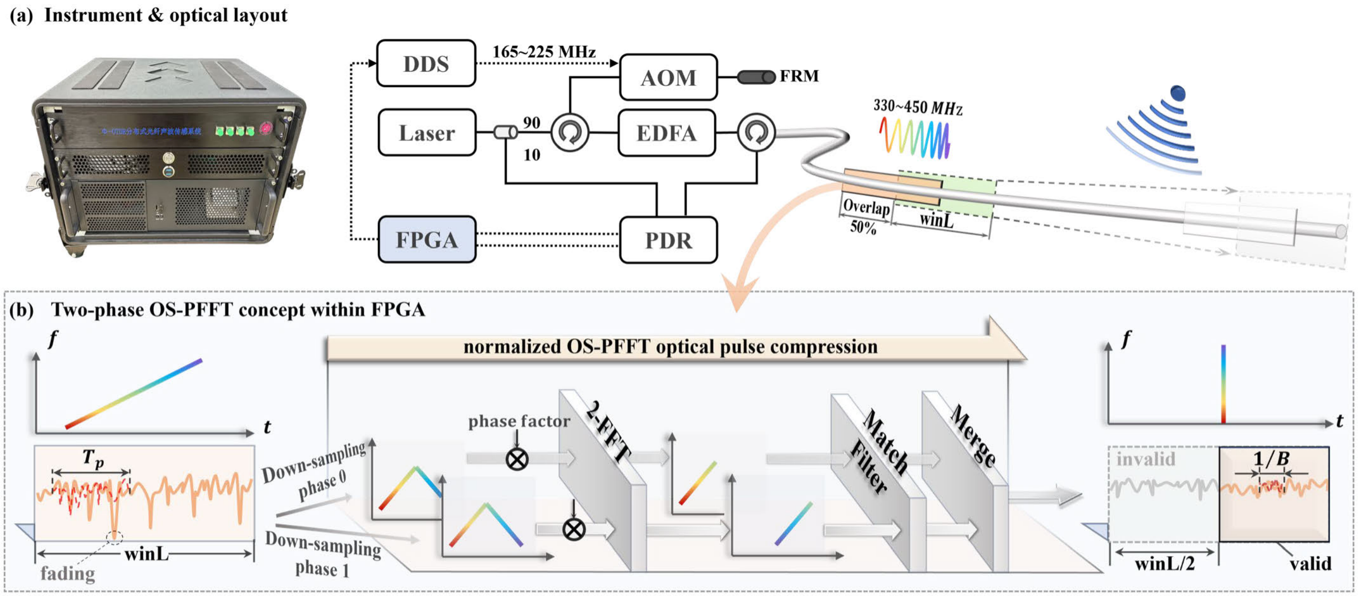

Fig. 1. Proposed CP Φ-OTDR interrogator and the OS-PFFT algorithm for DAS. (a) Photograph of the developed DAS instrument and its optical layout. (b) Schematic of the two-phase OS-PFFT concept for streaming pulse compression, enabling SNR/spatial-resolution improvement and mitigating fading. (OS-PFFT: overlap-save polyphase fast Fourier transform; AOM: acousto-optic modulator; FRM: Faraday rotator mirror; EDFA: erbium-doped fiber amplifier; PDR, polarization diversity receiver; and FPGA: field-programmable gate array).

the Hilbert transform of $i(t)$ to obtain the analytic signal $I(t)$, the pulse-compressed output $y(t)$ is given by the matched-filter operation

$$\begin{aligned} & y(t) \\ & = I(t) \otimes E^*(-t) \\ & = \int_0^{T_F} r(\tau) \exp(-j\omega_c \tau) \int_{-\infty}^{+\infty} \exp\left[j\left(\phi(\tau_{rt}-\tau)-\phi(\tau_{rt})\right]\right. \\ & \quad \cdot E(\tau_{rt}-\tau) E^*(\tau_{rt}-t)\, d\tau_{rt} d\tau \end{aligned} \tag{3}$$

where $\otimes$ is the convolution operator. Equation (3) gives the continuous-time matched-filter response of the RBS signal. In the following, the OS-PFFT architecture implements the matched filtering in (3) in a hardware-efficient way. For digital implementation, let $T_s = 1/f_s$ denote the sampling interval, and f_s is the sampling rate. The sampled analytic beat signal is defined as $x[n] = I(nT_s)$ and $h[n] = E^*(-nT_s)$, where $x[n]$ is the discrete input sequence and $h[n]$ is the sampled matched-filter kernel with effective length L_h. Then, with key notations summarized in Nomenclature, the sampled version of (3) is written as the discrete linear convolution

$$y[n] = \sum_{\ell}^{L_h-1} x[\ell]\, h[n-\ell]. \tag{4}$$

Equation (4) explicitly links the continuous-time matched filtering in (3) to its discrete-time FPGA implementation. However, directly evaluating (4) over a long FUT trace is unsuitable for real-time streaming. The overlap-save method is adopted as a block-convolution strategy to maintain a fixed transform size independent of trace length [35]. As shown in Fig. 1(b), let $winL$ denote the FFT block length, and let D denote the hop size between adjacent blocks. In general, $D = winL - (L_h - 1)$. In the present implementation, a 50% overlap is used, i.e., $D = winL/2$, and the design ensures that $L_h - 1 \le D$. Then, the bth input block can be defined and expressed as

$$x_b[u] = x[bD + u - (L_h - 1)] \tag{5}$$

where b is the block index and $u \in [0, winL - 1]$ is the local sample index within one block. Samples outside the valid range of $x[n]$ are set to zero. The matched-filtering implementation of the bth block convolution is then

$$y_b[u] = ifft_{winL}\left\{fft_{winL}\{x_b[u]\} \cdot * fft_{winL}\{h[u]\}\right\}. \tag{6}$$

Because the first $L_h - 1$ samples of each block output are corrupted by circular-convolution wraparound, only the valid part is retained. Accordingly, the global output sequence is reconstructed as

$$y[bD + n] = y_b[n + L_h - 1] \tag{7}$$

where $0 \le n \le D-1$, which corresponds to retaining the latter half of each computed segment in the present 50%-overlap implementation. By systematically discarding the wraparound artifacts and seamlessly concatenating these valid segments, (5)–(7) formulate the standard mechanism to continuously process the incoming beat signal. As a result, the computational complexity is governed by $winL$ rather than by the total number of samples in the FUT. In terms of hardware implementation, this blockwise strategy avoids the necessity of ultra-large-point FFTs, thereby significantly reducing the BRAM resource requirements.

To sustain the continuous 3.2-GSa/s ADC throughput where multiple samples arrive per clock cycle, the block FFT must be mapped onto a parallel polyphase architecture [36]. For the bth block, let $winL = MP$, where M is the number of polyphase branches and P is the FFT size in each branch. The $winL$-point FFT of $x_b[u]$ is

$$X_b\left[k\right] = \sum_{u=0}^{winL-1} x_b\left[u\right] W_{winL}^{uk} \tag{8}$$

where $W_N = \exp(-j2\pi/N)$ is the twiddle factor. By reindexing the time-domain sample index as $u = Mp + m$ and the frequency index as $k = k_1 + Pk_2$, where $0 \leq p,\ k_1 \leq P-1$ and $0 \leq m,\ k_2 \leq M-1$, (8) becomes

$$X_b\left[k_1 + Pk_2\right] = \sum_{m=0}^{M-1}\sum_{p=0}^{P-1} x_b\left[Mp + m\right] W_{winL}^{(Mp+m)(k_1+Pk_2)}. \tag{9}$$

Using the factorization property of the twiddle factors, the above expression can be rearranged as

$$X_b\left[k_1 + Pk_2\right] = \sum_{m=0}^{M-1} W_{winL}^{mk_1}\left(\sum_{p=0}^{P-1} x_b\left[Mp + m\right] W_{P}^{pk_1}\right) W_M^{mk_2}. \tag{10}$$

Equation (10) links this polyphase decomposition directly to the FPGA parallel architecture. The M parallel branches provide a natural mapping to the concurrent multiply-accumulate logic within DSP slices, enabling the system to sustain the massive 3.2-GSa/s ADC throughput.

Having established the hardware realization in (5)–(10), we next use the sampled matched-filter model in (4) to interpret the sensing performance. Using the known relation $\mathbb{E}\{\exp[j(\phi(t-\tau)-\phi(t)]\} = \exp(-2\pi\Delta\nu\tau)$ [37], the mean measurement response of $y[n]$ can be rewritten as

$$\mathbb{E}\left\{y\left[n\right]\right\} = \sum_{\ell} r\left[\ell\right]\exp\left(-j\omega_c \ell T_s\right)\exp\left(-2\pi\Delta\nu\ell T_s\right) q\left[n-\ell\right] \tag{11}$$

where $\Delta\nu$ is the linewidth of the laser source, $r[\ell] = r(\ell T_s)$ denotes the sampled RBS sequence, and $q[n]$ is the discrete pulse-compression kernel, i.e., the sampled autocorrelation of the chirped pulse. Equation (11) shows that the sampled output inherits both the autocorrelation profile of the chirped pulse and the distance-dependent linewidth penalty. Let $z_n = v_g n T_s/2$ denote the distance corresponding to the nth sampled position, where v_g is the group velocity in the fiber. The phase-extraction noise variance at position z_n can be expressed as [37]

$$\sigma_\theta^2\left(z_n\right) = \frac{1}{SNR\left(z_n\right)} \approx \frac{q_e B}{R_d P_y\left(z_n\right)} \frac{1}{\exp^2\left(-2\pi\Delta\nu n T_s\right)} \tag{12}$$

where R_d is the responsivity of the detector, q_e is the electron charge, $P_y(z_n)$ is the local power of the sampled pulse-compressed output at position z_n, and B is the equivalent noise bandwidth of $q[n]$. Considering band-limited white noise, the sampled noise variance after repeated interrogation with an interval T_F is

$$\sigma_d^2\left(z_n\right) = 2\Delta f \sigma_\theta^2\left(z_n\right) T_F \tag{13}$$

where $\Delta f$is the bandwidth of the band-limited white noise with the condition $\Delta f \cdot T_F \geq 1$. Equation (13) further indicates that operating a practical OTDR system at the highest feasible pulse repetition frequency is beneficial for enhancing detection sensitivity and improving adaptability in complex scenarios.

III. EXPERIMENTAL SETUP

Fig. 1(a) shows the experimental setup of the proposed CP Φ-OTDR. In this system, the light wave from a narrow linewidth laser (NKT, E15) is split into two beams by a 90:10 optical coupler. The probe beam (90%) is periodically modulated into optical pulses with a width of 1 μs and a period of 100 μs by an acousto-optic modulator (AOM), while the reference beam (10%) remains a frequency-stable continuous light wave. The AOM is driven by a DDS with a frequency sweeping range from 165 to 225 MHz. A double-pass configuration with a Faraday rotator mirror (FRM) is used to increase the light-wave frequency chirp rate. After two interactions with the AOM, the probe beam chirps from 330 to 450 MHz before being amplified by an erbium-doped fiber amplifier (EDFA). Then, the probe pulse is launched into FUT via an optical circulator. The RBS signal from the FUT is sent to the polarization diversity receiver (PDR), where its two orthogonal polarization states mix with the LO, respectively. Subsequently, the two beating signals are converted into electrical signals by a pair of balanced photodetectors (BPDs, 1.6-GHz bandwidth) and then sampled by a dual-channel high-speed ADC (ADC12DJ3200, 3.2 GSa/s, 12-bit resolution) with a full-scale voltage of 1 V.

As shown in Fig. 2(a), the sampled beat signal is streamed into the FPGA for real-time demodulation. Fig. 2(b) details the M-phase FFT decomposition and frequency-domain matched filtering for pulse compression. A $winL$-sample data segment is partitioned into M phases with step M, each undergoing a P−point FFT, multiplication by the phase shift factor $W_{winL}^{k_1 m}$, and then an M−point FFT applied across the Msamples simultaneously produced by the M channels at each clock cycle. Each channel's output corresponds to frequency-domain points spaced by P, with pulse compression achieved by multiplying these outputs with matched filter coefficients. The corresponding spectrogram before/after compression is illustrated in Fig. 2(c). In the experiment, $M = 16$ and $L = 2$ are set, where L denotes the number of selected phases. The first and second phases (200–600 MHz) are employed for the L−phase IFFT, generating time-domain complex signals at a 400-MSa/s sampling rate. This procedure is equivalent to applying an eight-point moving average followed by eightfold downsampling to signals from the M−phase IFFT, thereby enhancing SNR [38]. At a 3.2-GSa/s sampling rate, the proposed method avoids an M−phase IFFT after the M−phase FFT by exploiting the confinement of the RBS signal to 330–450 MHz. Since out-of-band components are suppressed by matched filtering, truncating the spectrum to 200–600 MHz for the L−phase IFFT significantly improves computational efficiency while introducing negligible distortion. Subsequently, the inner-pulse frequency-division (IPFD) method and the rotated-vector-summary (RVS) method are [39] used to fuse orthogonally polarized signals. Finally, the FPGA-processed demodulated phase is transferred to the host computer for storage, with the sampling duration limited only by the storage capacity.

IV. RESULTS AND DISCUSSION

The influence of the number of FFT points and the chirped pulse duration on signal reconstruction was studied. The

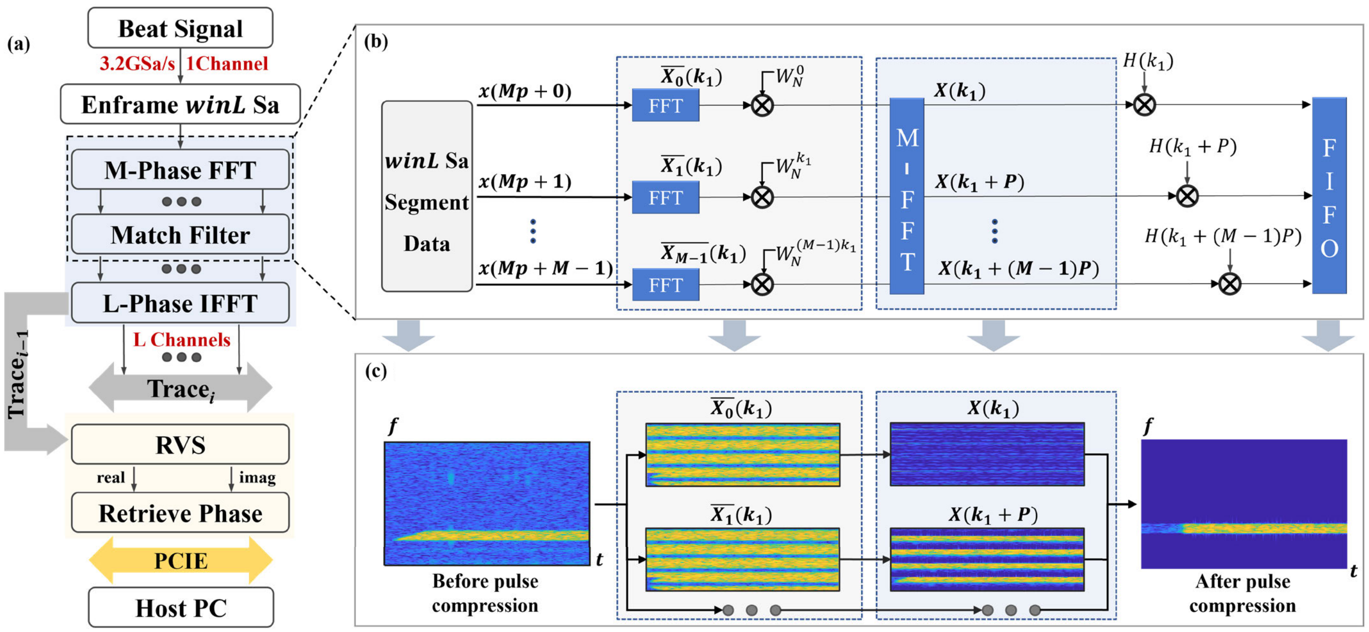

Fig. 2. Data processing flow of CP Φ-OTDR demodulation with the OS-PFFT algorithm implemented in an FPGA. (a) Processing pipeline from beat-signal sampling to phase retrieval. (b) Zoom-in of the M-phase FFT and frequency-domain matched filtering. (c) Spectrogram illustration before and after pulse compression. (OS-PFFT: overlap-save polyphase fast Fourier transform; RVS: rotated vector summary).

number of FFT points was set to 2048, 4096, 8192, 16 384, 32 768, and 65 536, respectively, and the pulsewidth was set to 500, 1000, 2000, and 5000 ns, respectively. An FFT operation with stagewise scaling was performed based on the radix-2 butterfly structure [40]. For RBS data with varying pulse widths, frequency-domain pulse compression is performed using double-precision arithmetic to obtain references, where the number of FFT points is determined by the temporal length of the chirped pulse. The demodulation accuracy of the OS-PFFT optical pulse compression across different FFT point configurations is evaluated via Pearson correlation coefficients (PCCs) and root-mean-square error (RMSE) between its results and the references. As depicted in Fig. 3(a) and (b), PCCs increase monotonically, while RMSE decreases with increasing FFT points. Theoretically, when the FFT point count reaches twice the CP duration and approaches the nearest power of two, the consistency between the demodulated results and reference signals improves significantly. However, due to quantization errors, further increases in FFT points lead to performance degradation. In addition, Fig. 3(c) illustrates that larger FFT point sizes result in higher FPGA resource utilization.

In our implementation on an Xilinx KU060 FPGA, the OS-PFFT scheme with *winL* = 8192 and *M* = 16 consumes 12.94% LUTs, 9.39% LUTRAM, 12.76% FFs, 8.74% BRAMs, and 33.56% DSP slices, whereas a direct 8192-point FFT consumes only 5.84% LUTs, 3.57% LUTRAM, 5.81% FFs, 8.34% BRAMs, and 9.90% DSPs. The OS-PFFT scheme delivers a 16× throughput gain while remaining deployable on commercial FPGAs through appropriate parameter selection. For operation at even higher ADC sampling rates, the throughput can be further increased by partitioning the OS-PFFT into a larger number of parallel polyphase branches so that more samples are processed per clock cycle. In such cases, additional timing constraints and careful placement are required to ensure interphase synchronization and preserve phase coherence across the reconstructed RBS traces.

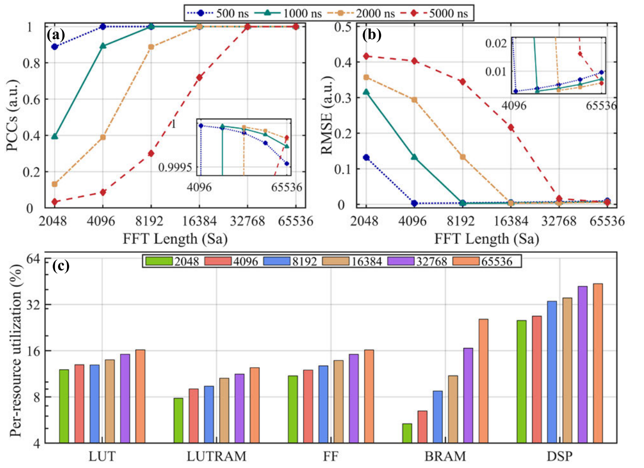

Fig. 3. Influence of different FFT points on the reconstruction accuracy and resource consumption for RBS pulse compression. (a) PCCs and (b) RMSE accuracy of RBS for chirped pulses of 500, 1000, 2000, and 5000 ns using FFT points from 2048 to 65 536. (c) Per-resource FPGA utilization of the DAS demodulation algorithm with different FFT points. The percentages represent the utilization of each resource type relative to the corresponding total available resources.

Subsequently, we analyzed the influence of *winL* on the demodulation. Considering that the total length of the FUT was nearly 9 km, the duration of chirped pulse was set to 1 μs, and a repetition period was set to 100 μs, slightly larger than the maximum round-trip time of lightwave traveling through the FUT. Besides, the gauge length of this system was configured to 0.9 m. A cylinder piezoelectric transducer (PZT), with an approximately 80-cm-long fiber attached, was placed at 8395 m and was excited by a 1-kHz sinusoidal

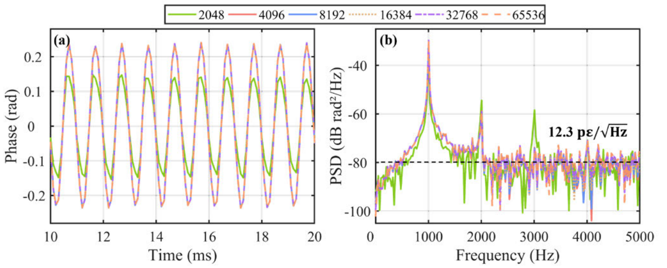

Fig. 4. (a) Measurement results of 1-kHz vibration with different FFT points and (b) corresponding PSDs.

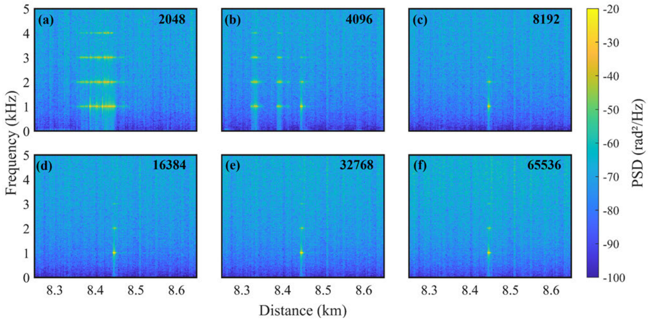

Fig. 5. PSD of dynamic strain along the fiber for the RBS of a chirped pulse with a duration of 1 μs when using different FFT points for pulse compression: (a) 2048, (b) 4096, (c) 8192, (d) 16 384, (e) 32 768, and (f) 65 536.

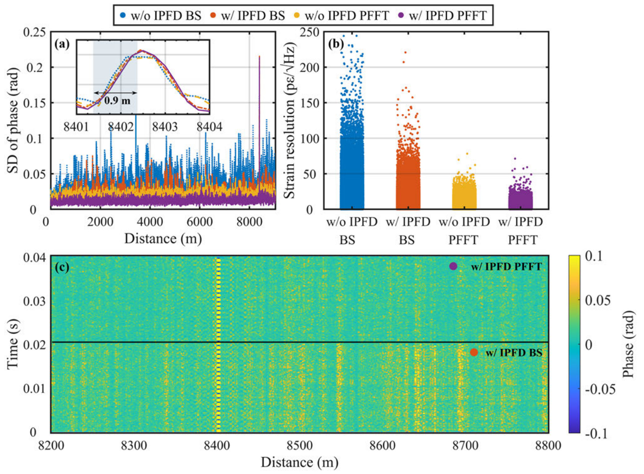

Fig. 6. DAS demodulation results using the OS-PFFT and BS method with the same original dataset (0.04-s, 400 temporal samples). (a) Phase standard deviation as functions of distances, (b) strain resolution, and (c) phase-distance traces. (IPFD: inner-pulse frequency-division; BS: bandpass sampling; and OS-PFFT: overlap-save polyphase fast Fourier transform).

signal. The recovered waveforms and power spectral densities (PSDs), with a recording time of 0.4 s, are plotted in Fig. 4(a) and (b). The results show little discrepancy in either the time or frequency domain, except when *winL* is 2048. As shown in Fig. 4(a), when *winL* is larger than 2048, the time-domain waveforms with period of 1 ms and the amplitude of 0.24 rad are successfully reconstructed. As shown in Fig. 4(b), when *winL* is larger than 2048, the PSDs show fewer higher-order harmonics, and the strain resolution is nearly 12.3 p$\varepsilon/\sqrt{\text{Hz}}$. Besides, improper *winL* configuration induces spatial crosstalk. As shown in Fig. 5(a), $winL = 2048$ results in crosstalk spanning ~150 m at vibration region, accompanied by prominent higher-order harmonics. Increasing *winL* to 4096 [see Fig. 5(b)] can partially suppress the crosstalk and harmonic distortions though full pulse compression remains unachieved. Further increasing *winL* [see Fig. 5(c)–(f)] shows that when $winL \geq 8192$, nonvibrating regions exhibit no significant frequency components in range-frequency plots, indicating a stable operational state. This phenomenon arises due to spectral aliasing from consecutive data segments: when the number of FFT points is less than twice the pulsewidth, aliasing introduces vibration-related artifacts into undisturbed regions, leading to spatial crosstalk and elevated harmonics.

Next, demodulations using the proposed OS-PFFT method and the bandpass-sampling (BS) method were performed on the same original dataset. The detailed procedure of the OS-PFFT method has been described in Section III, with parameters $winL = 8192$ and $P = 512$. In the bandpass sampling scheme, the signal is first upconverted above 110 MHz, filtered by a finite impulse response (FIR) filter with a 440–560-MHz passband (cutoffs at 400 and 600 MHz, and sideband suppression ratio of 30 dB) and then downsampled from 3.2 to 400 MSa/s. The inset of Fig. 6(a) verifies that both approaches reach a spatial resolution of 0.9 m. However, OS-PFFT consistently exhibits lower phase fluctuations along the fiber, resulting in a distribution with reduced variance and lower mean strain resolution, as shown in Fig. 6(b). Although the IPFD algorithm suppresses noise for both methods, its effect on OS-PFFT is marginal, and OS-PFFT still outperforms BS with IPFD even without the aid of IPFD. As illustrated in Fig. 6(c), this benefit is further reflected in reduced phase fluctuations across both the spatial and temporal distributions of the demodulated acoustic signals. These results confirm that OS-PFFT achieves superior sensing performance by exploiting the dense spatial information of high sampling-rate ADCs instead of discarding it.

In addition, we evaluated the long-distance sensing capability of the proposed DAS system. First, a dual-source vibration experiment was conducted to further verify the system's spatial resolvability. Two PZT stack actuators (~2 cm) were bonded with the sensing fiber using epoxy adhesive and placed at ~8.4 km. As shown in Fig. 7(a) and (b), two vibration sources spaced by 2.25 m can be clearly distinguished in both the spatiotemporal and frequency–spatial domains. To quantify the practical distinguishability, additional measurements were performed with only PZT1 or only PZT2 driven, and the spatial distributions of the corresponding mean PSDs above 25 Hz were extracted, as shown in Fig. 7(c). The response at the other PZT position drops to approximately −77.03 dB rad^2/Hz, which is statistically consistent with the mean spatial background noise floor of −83.08 dB rad^2/Hz (with a spatial standard deviation $\sigma \approx 5.01$ dB). Since the off-target energy lies within 1.2σ of the mean background noise, any residual crosstalk is effectively buried beneath the noise floor. Consequently, an average peak-to-background contrast of 15.4 dB is achieved. This margin corresponds to a 3.1σ statistical confidence level, ensuring a clear discrimination between the two vibration sources. To illustrate this statistical context, a shaded band representing the mean background noise floor and its ±1σ bounds is included in Fig. 7(c).

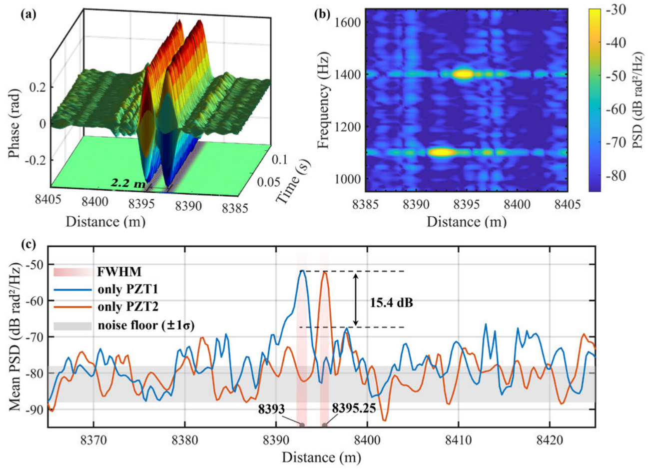

Fig. 7. Dual-source vibration experiment for validating spatial resolvability. The two sources were excited at 1100 and 1400 Hz, respectively. (a) Demodulated vibration responses in the spatiotemporal domain. (b) Frequency–spatial map obtained from the channelwise PSDs (0.12-s, 1200 temporal samples). (c) Spatial distributions of the extracted mean PSDs for the single-source cases (“only PZT1” and “only PZT2”). The shaded regions indicate the −3-dB widths (FWHMs) of the spatial peaks, and the dashed lines mark the peak-to-off-target contrast of 15.4 dB.

In addition, the extracted spatial peaks exhibit −3-dB widths (FWHMs) of approximately 1.25 m for PZT1 and 1.0 m for PZT2. Although their 0.25-m difference is constrained by the spatial sampling interval, the 15.4-dB (3.1σ) peak-to-background margin confirms that interchannel crosstalk is suppressed to the ambient noise floor, ensuring clear spatial resolvability at this distance. Then, experiments were performed with FUT lengths of 10, 25, 50, and 70 km. For each configuration, the PZT was positioned at 8.4, 23.1, 49.4, and 69.1 km, with the corresponding pulse repetition rates set to 10, 4, 2, and 1.25 kHz, respectively. Fig. 8(a) depicts the phase standard deviations across the entire FUT, which serve to characterize the system’s spatial resolution at different sensing ranges. The insets of Fig. 8(a) confirm that the system preserves a 0.9-m spatial resolution up to 25 km, with the resolution gradually relaxing to 1.75 m at 50 km and 2.5 m at 70 km. This gradual relaxation is primarily attributed to the distance-dependent increase of phase-extraction noise, which causes the matched-filter response to deviate from the ideal autocorrelation and broadens the correlation peak [see (11) and (12)]. To further quantify the performance of our system, the probability density functions of strain resolution were calculated from the corresponding PSDs above 25 Hz and integrated to obtain the cumulative distribution functions (CDFs). As shown in Fig. 8(b), the median strain sensitivity for a 10-km FUT is 8.9 $\text{p}\varepsilon/\sqrt{\text{Hz}}$. With increasing sensing distance, more far-end channels with higher noise accumulation are included, which reduces sensitivity. The median values are 26.3, 57.5, and 72.4 $\text{p}\varepsilon/\sqrt{\text{Hz}}$ at 25, 50, and 70 km, respectively. The equivalent strain resolutions, defined as the 99% full width of the CDF, are 35.9, 124.4, 346.7, and 732.8 $\text{p}\varepsilon/\sqrt{\text{Hz}}$ for the four tested configurations. The results validate the proposed DAS system’s capability to deliver submeter spatial resolution up to 25 km while maintaining reliable strain sensitivity at longer sensing ranges.

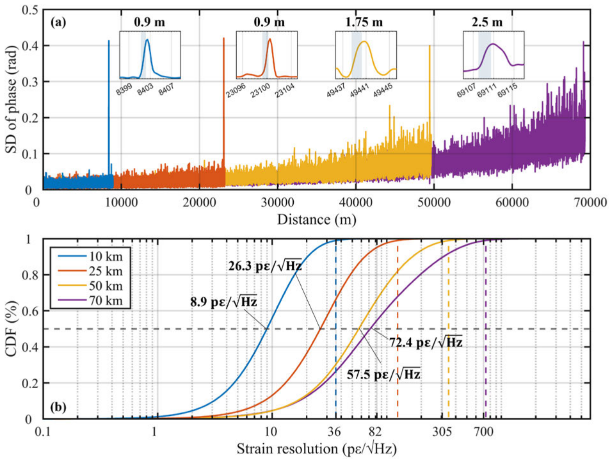

Fig. 8. Strain resolution of the proposed DAS system at FUT lengths of 10, 25, 50, and 70 km. (a) Phase standard deviation along the FUT. (b) CDFs of strain sensitivity.

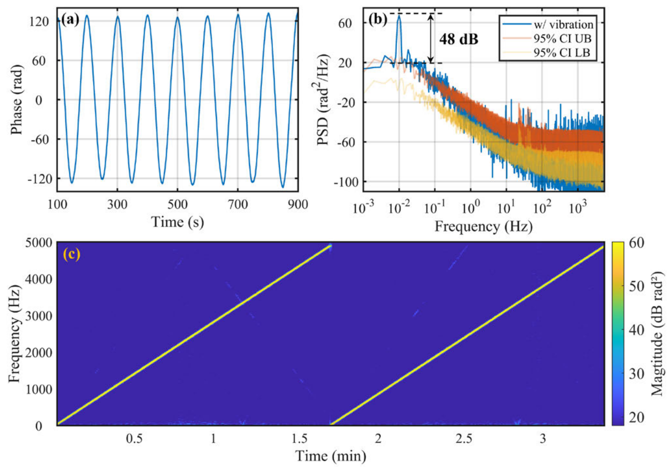

Fig. 9. Vibration waveform recovered at 8400 m with frequency of (a) 0.01 Hz and (b) its PSD and the 95% CI of background noise. (c) Time–frequency graph of the sweeping frequency waveform recovered. (CI: confidence interval).

Finally, the long-term monitoring capability of our DAS system was examined. By maintaining a pulse repetition frequency of 10 kHz/s to minimize the noise power density of the DAS data stream [7], the demonstration system recorded data over 1000 s, with a PZT placed at 8400 m driven at 0.01 Hz. The excitation was generated by a piezoelectric ceramic PZT drive controller module (KDT350AMPDIFF-003) and applied to a tube-type PZT with the sensing fiber tightly wound around it to introduce sinusoidal strain modulation. In Fig. 9(a), a 0.01-Hz sinusoidal signal was correctly restored. For PSD analysis, a quiet region near the PZT was used, and the 95% confidence interval (CI) of background noise was taken as the reference. As shown in Fig. 9(b), the PSD of the 10-mHz time-domain signal, over a broad bandwidth ranging from 0.001 to 5000 Hz, exhibits a high SNR of nearly 48 dB at 0.01 Hz. Besides, an acoustic wave whose frequency swept from 1 to 4900 Hz and a period of 100 s was generated by PZT. Fig. 9(c) illustrates the time–frequency variation diagram of two complete frequency sweep cycles, where the frequency components at different

TABLE I

KEY PERFORMANCE METRICS OF THE DAS SYSTEM

Method	Sample spacing	Sensing range	Spatial resolution	Frequency response range	Noise evaluation band	Sensitivity (CDF at 50%)	Sensitivity (CDF at 99%)	Organization
Conventional Φ-OTDR [42]	25 cm	50 km	3 m @ 30 km 30 m @ 50 km	1 mHz ~ 50 kHz	@ 1 kHz	272 μrad/√Hz	-	Silixa Ltd. (iDAS^{TM})
Φ-OTDR using dual-soliton microcombs [43]	-	72 km	5 m	5 Hz ~ 5 kHz	> 500 Hz	20.8 μrad/√Hz @ 10 km	-	UESTC
TGD-OFDR [44]	20 cm	120 km	1 m @ 80 km	0.1 Hz ~ 10 kHz	-	181 μrad/√Hz @ 20 km	-	Neubrex Co., Ltd. (NBX-S4100)
Chirped-pulse Φ-OTDR [45]	33 cm	10 km 100 km	10 m	-	> 50 Hz 10 ~ 238 Hz	134 μrad/√Hz 4.5 mrad/√Hz	193 μrad/√Hz* -	ASN Ltd. (OptoDAS)
Chirped-pulse Φ-OTDR with PNC [46]	-	50 km	4.24 m	-	-	-	1.46 mrad/√Hz	SJTU
Chirped-pulse Φ-OTDR with OS-PFFT	3.125 cm	10 km 25 km 50 km 70 km	0.9 m 0.9 m 1.75 m 2.5 m	0.01 Hz ~ 5 kHz	> 25 Hz	72.5 μrad/√Hz 214.5 μrad/√Hz 911.5 μrad/√Hz 1.6 mrad/√Hz	292 μrad/√Hz 1.0 mrad/√Hz 5.5 mrad/√Hz 16.6 mrad/√Hz	This work

* Value reported at 90% CDF (others at 99% CDF).

moments can be accurately detected, with a harmonic suppression ratio exceeding 40 dB. The subtle signal in Fig. 9(c) corresponds to the secondary harmonics induced by PZT vibrations, which follow the same linear trend and periodicity. Then, a 10-h continuous monitoring test was conducted on a 160-m fiber section (8390–8560 m) to assess system stability under realistic environmental conditions. The results, shown in Fig. 10, fully characterize the system's detection capability across the entire frequency range. In Fig. 10(a), the system achieves an ASD of 1 $\mu\varepsilon/\sqrt{\text{Hz}}$ at 1 mHz and falls below 10 p$\varepsilon/\sqrt{\text{Hz}}$ in the high-frequency region. The low-frequency rise exhibits a 1/f-like characteristic. As widely reported in recent literature [11], [41], such spectral behavior in the subhertz regime is highly consistent with the phase noise induced by laser-frequency drift and ambient temperature fluctuations, which poses a persistent limitation for ultralow-frequency detection in DAS systems. The excess noise observed in the 10–500-Hz band is likely dominated by environmental acoustic/mechanical disturbances in the laboratory, such as door openings, air conditioning, and fan operating sounds. At higher frequencies, the ASD approaches a white-noise-limited floor. The Allan deviation in Fig. 10(b) shows an approximately -0.5 slope in the short-τ region, which is consistent with white phase noise. Importantly, no slope of -1 is observed, indicating that quantization noise is not the dominant limitation of the present system. The upward trend at longer τ, with a slope approaching + 0.5, reflects slow environmental drift and low-frequency fluctuations accumulated overextended averaging times. In addition, the system can sustain real-time demodulation overextended periods without compromising frequency response bandwidth. Longer recordings require only increased disk storage, avoiding issues such as data overflow or memory limitations.

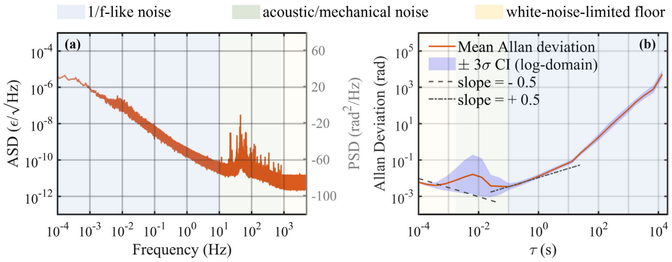

Fig. 10. Ten-hour stability characterization of the DAS system over 640 time-series samples. (a) Mean background strain ASD, with representative dominant noise regimes annotated. (b) Allan deviation versus averaging time τ, with reference slopes of -0.5 and $+\ 0.5$ shown for comparison. (Shaded: 3σ interval).

To place our results in context, Table I compares representative DAS implementations with the proposed system in terms of sensing range, spatial resolution, frequency response, and sensitivity (cdf at 50% and 99%, respectively). For consistency of presentation, the sensitivity values in Table I are reported in rad/$\sqrt{\text{Hz}}$. When the original sources provide strain sensitivity in p$\varepsilon/\sqrt{\text{Hz}}$, the values are converted to equivalent phase sensitivity using the reported spatial resolution and the coefficient $K = 110.37$ nε·m/rad [47]. The resulting values are intended for contextual comparison and should be interpreted under the reported evaluation conditions of the respective references. At 10 km, under the respective reported conditions, our system achieves higher sensitivity than the commercial OptoDAS [45] but remains slightly below the dual-soliton microcomb–based DAS [43]. At 25 km, with a noise evaluation band above 25 Hz, the system maintains submeter resolution and achieves a sensitivity of 214.5 μrad/$\sqrt{\text{Hz}}$, demonstrating competitive performance at this distance. At 50 km, the reported 50% cdf sensitivity is comparable to that in [46] under a similar NKT E15 laser condition, whereas [46] reports a better 99% cdf result in conjunction with phase–noise compensation. At longer sensing distances, finer spatial resolution is reported for the NBX-S4100 [44], and lower sensitivity values are reported for the OptoDAS [45]. These differences should be interpreted together with differences in fiber type and averaging configuration. For example, the present implementation uses standard SMF and a sliding window constrained to the gauge length, whereas the OptoDAS result is reported with a 200-m sliding-average window that substantially exceeds the gauge length. In terms of ultralow-frequency detection, iDAS-MG[1] [42] reports operation down to 0.001 Hz, whereas our system

---

[1] Trademarked.

demonstrates detection at 0.01 Hz. Table I provides a contextual comparison between the proposed system and representative DAS implementations under their respective reported conditions. The experimental results above demonstrate the practical capability of the OS-PFFT-based real-time approach for DAS sensing. The system supports operation from the sub-Hz range (geohazard monitoring [48]) to the kHz range (pipeline leakage detection, 1–2 kHz [1], [49]), making it highly versatile across diverse applications. Its ability to detect both high-frequency features and ultralow-frequency signals demonstrates its broad operational bandwidth, a key advantage for real-time, long-distance monitoring.

V. CONCLUSION

In this article, a real-time FPGA digital signal processing scheme based on the OS-PFFT pulse compression technique was presented and validated. This approach significantly enhances data throughput to meet the compression requirements at a sampling rate of 3.2 GSa/s, decoupling the length of the FUT from the computational burden. Proof-of-concept experiments verified a spatial resolution of 0.9 m up to 25 km with a sensitivity of 214.5 μrad/$\sqrt{\text{Hz}}$ while achieving spatial resolutions of 1.75 m at 50 km and 2.5 m at 70 km. In addition, a 10-mHz low-frequency signal was successfully recovered with an SNR of approximately 48 dB, and the system stability was validated by continuous operation for 10 h at a 0.1-ms refresh rate. Moreover, the proposed OS-PFFT-based scheme can be combined with silicon-photonic interrogators for DAS, such as the integrated interrogator in [50], potentially enabling monolithic modulation–demodulation on a hybrid photonic–electronic platform. Overall, this work holds broad application prospects. For example, in oil well extraction, it measures low-frequency signals from slow geological structural changes and high-frequency sounds from fluid turbulence. In mountain structural monitoring, it enables early landslide detection and monitors forest flora/fauna activities, highlighting its versatility across real-world applications.

REFERENCES

[1] T. Li et al., “Nonintrusive distributed flow rate sensing system based on flow-induced vibrations detection,” *IEEE Trans. Instrum. Meas.*, vol. 70, pp. 1–8, 2021.

[2] P. Wang et al., “Partial discharge measurement for power cable using crosstalk-free FDM-DAS,” *IEEE Trans. Instrum. Meas.*, vol. 73, pp. 1–10, 2024.

[3] X. Chen et al., “On-line status monitoring and surrounding environment perception of an underwater cable based on the phase-locked Φ-OTDR sensing system,” *Opt. Exp.*, vol. 30, no. 17, p. 30312, Aug. 2022.

[4] F. Peng et al., “Vehicle trajectory extraction from weak and discontinuous quasi-static DAS signals using a multi-scale context Pix2pix,” *IEEE Trans. Instrum. Meas.*, vol. 74, pp. 1–11, Jan. 2025.

[5] Y. Wu et al., “Rapid deployment of traffic monitoring system: high-fidelity DAS for capturing heterogeneous traffic features,” *IEEE Trans. Intell. Transp. Syst.*, early access, Feb. 27, 2026, doi: 10.1109/TITS.2026.3666682.

[6] A. Ellmauthaler, M. LeBlanc, J. Bush, M. E. Willis, J. L. Maida, and G. A. Wilson, “Real-time DAS VSP acquisition and processing on single - and multi-mode fibers,” *IEEE Sensors J.*, vol. 21, no. 13, pp. 14847–14852, Jul. 2021.

[7] S. Huang, Q. Chai, G. Xiao, and J. Zhang, “Identification and prediction of low flow rate based on time-shift statistical feature enhancement with DAS,” *IEEE Trans. Instrum. Meas.*, vol. 74, pp. 1–7, 2025.

[8] T. Liu et al., “Ultra-high resolution strain sensor network assisted with an LS-SVM based hysteresis model,” *OEA*, vol. 4, no. 5, May 2021, Art. no. 200037.

[9] Y. Wang, P. Lu, S. Mihailov, L. Chen, and X. Bao, “Ultra-low frequency dynamic strain detection with laser frequency drifting compensation based on a random fiber grating array,” *Opt. Lett.*, vol. 46, no. 4, pp. 789–792, Feb. 2021.

[10] P. J. Vidal-Moreno et al., “Cancellation of reference update-induced 1/f noise in a chirped-pulse DAS,” *Opt. Lett.*, vol. 47, no. 14, pp. 3588–3591, Jul. 2022.

[11] G. Zhu, F. Liu, W. Kong, X. Yang, S. Kumar, and X. Zhou, “Low-frequency vibration detection enhancement in dual-pulse DAS with single AOM,” *IEEE Trans. Instrum. Meas.*, vol. 73, pp. 1–8, 2024.

[12] M. Zabihi and K. Krebber, “Laser source frequency drift compensation in Φ-OTDR systems using multiple probe frequencies,” *Opt. Exp.*, vol. 30, no. 11, p. 19990, May 2022.

[13] S. Liu et al., “Quantitative demodulation of distributed low-frequency vibration based on phase-shifted dual-pulse phase-sensitive OTDR with direct detection,” *Opt. Exp.*, vol. 30, no. 6, pp. 10096–10109, Mar. 2022.

[14] F. Yu et al., “Data reduction in phase-sensitive OTDR with ultra-low sampling resolution and undersampling techniques,” *Sensors*, vol. 22, no. 17, p. 6386, Aug. 2022.

[15] G. Zhu, F. Liu, X. Liu, S. Kumar, and X. Zhou, “Noise performance analysis and optimization of downsampling heterodyne Φ-OTDR,” *IEEE Sensors J.*, vol. 24, no. 9, pp. 14093–14100, May 2024.

[16] F. Jiang et al., “Undersampling for fiber distributed acoustic sensing based on coherent phase-OTDR,” *Opt. Lett.*, vol. 44, no. 4, pp. 911–914, Feb. 2019.

[17] Z. Ye, S. Zhang, A. Wan, J. Zhang, and Z. Wang, “The impact of quantization bits on coherent detection DAS,” *J. Lightw. Technol.*, vol. 42, no. 10, pp. 3936–3943, May 15, 2024.

[18] F.-H. Yu et al., “Ultra-low sampling resolution technique for heterodyne phase-OTDR based distributed acoustic sensing,” *Opt. Lett.*, vol. 47, no. 14, pp. 3379–3382, Jul. 2022.

[19] N. Xue, Y. Fu, C. Lu, J. Xiong, L. Yang, and Z. Wang, “Characterization and compensation of phase offset in Φ-OTDR with heterodyne detection,” *J. Lightw. Technol.*, vol. 36, no. 23, pp. 5481–5487, Dec. 1, 2018.

[20] Y. Fu, N. Xue, Z. Wang, B. Zhang, J. Xiong, and Y. Rao, “Impact of I/Q amplitude imbalance on coherent Φ-OTDR,” *J. Lightw. Technol.*, vol. 36, no. 4, pp. 1069–1075, Feb. 15, 2018.

[21] Z. Wang et al., “Coherent Φ-OTDR based on I/Q demodulation and homodyne detection,” *Opt. Exp.*, vol. 24, no. 2, p. 853, Jan. 2016.

[22] G. Tu, M. Zhao, B. Yu, and J. Lin, “A phase-sensitive optical time-domain reflectometry system with an electrical I/Q demodulator,” *Proc. SPIE*, vol. 8311, p. 78, Oct. 2018.

[23] F. Jiang et al., “Low computational cost distributed acoustic sensing using analog I/Q demodulation,” *Sensors*, vol. 19, no. 17, p. 3753, Aug. 2019.

[24] F. Zhou et al., “A real-time phase processing system for phase sensitive optical time domain reflectometer,” *Rev. Scientific Instrum.*, vol. 94, no. 1, Jan. 2023, Art. no. 014710.

[25] F. Calliari, M. M. Correia, G. P. Temporão, G. C. Amaral, and J. P. V. D. Weid, “Fast acquisition tunable high-resolution photon-counting OTDR,” *J. Lightw. Technol.*, vol. 38, no. 16, pp. 4572–4579, Aug. 15, 2020.

[26] Q. Sheng, Z. Yu, B. Lu, Z. Li, Q. Ye, and Z. Zhang, “Real-time phase-sensitive optical time-domain reflectometry signal processing system based on heterogeneous accelerated computing,” *Chin. J. Lasers*, vol. 47, no. 1, 2020, Art. no. 0104002.

[27] Z. Sha, H. Feng, Y. Shi, and Z. Zeng, “Phase-sensitive optical time domain reflectometer with ultrafast data processing based on GPU parallel computation,” *Appl. Opt.*, vol. 57, no. 10, p. 2679, Mar. 2018.

[28] K. Kishida et al., “Development of real-time time gated digital (TGD) OFDR method and its performance verification,” *Sensors*, vol. 21, no. 14, p. 4865, Jul. 2021.

[29] D. Hillerkuss et al., “Simple all-optical FFT scheme enabling tbit/s real-time signal processing,” *Opt. Exp.*, vol. 18, no. 9, p. 9324, Apr. 2010.

[30] R. G. Rozier, F. E. Kiamilev, and A. V. Krishnamoorthy, “Design and evaluation of a photonic FFT processor,” *J. Parallel Distrib. Comput.*, vol. 41, no. 1, pp. 131–136, Feb. 1997.

[31] K. Hosseini et al., “8 tbps co-packaged FPGA and silicon photonics optical IO,” in *Proc. Opt. Fiber Commun. Conf. Exhib. (OFC)*, Jun. 2021, pp. 1–3.

[32] C. Zhou, Q. Meng, W. Liu, S. Guo, H. Zhang, and G. Li, “Multisegment overlap–save method for coherent dedispersion,” *Astronomical J.*, vol. 168, no. 6, p. 254, Nov. 2024.

[33] J. D. Bunton et al., “Performance of oversampled polyphase filterbank inversion via Fourier transform: Continuous signals,” *J. Astronomical Instrum.*, vol. 10, no. 4, Nov. 2021, Art. no. 2050004-444.

[34] A. Loayssa, M. Sagues, and A. Eyal, "Phase noise effects on phase-sensitive OTDR sensors using optical pulse compression," *J. Lightw. Technol.*, vol. 40, no. 8, pp. 2561–2569, Apr. 15, 2022.

[35] M. Borgerding, "Turning overlap-save into a multiband mixing, downsampling filter bank," *IEEE Signal Process. Mag.*, vol. 23, no. 2, pp. 158–161, Mar. 2006.

[36] Y. Y. Zhang, L. Zhang, Z. Q. Shang, Y. R. Su, Z. Wu, and F. B. Yan, "A new multichannel parallel real-time FFT algorithm for a solar radio observation system based on FPGA," *Publications Astronomical Soc. Pacific*, vol. 134, no. 1033, Mar. 2022, Art. no. 034502.

[37] J. Li et al., "Influence of laser linewidth on phase-OTDR system based on heterodyne detection," *J. Lightw. Technol.*, vol. 37, no. 11, pp. 2641–2647, Jun. 1, 2019.

[38] H. Li et al., "Spatio-temporal joint oversampling-downsampling technique for ultra-high resolution fiber optic distributed acoustic sensing," *Opt. Exp.*, vol. 30, no. 16, pp. 29639–29654, Jul. 2022.

[39] D. Chen, Q. Liu, and Z. He, "Phase-detection distributed fiber-optic vibration sensor without fading-noise based on time-gated digital OFDR," *Opt. Exp.*, vol. 25, no. 7, pp. 8315–8325, Mar. 2017.

[40] C. Van Loan, *Computational Frameworks for the Fast Fourier Transform*. Philadelphia, PA, USA: SIAM, 1992.

[41] C. Wang, X. Gui, X. Fu, Y. Wang, C. He, and Z. Li, "CFBG enhanced distributed acoustic sensing covering millihertz to kilohertz band," *Opt. Laser Technol.*, Jun. 2024, Art. no. 112448.

[42] C.-R. Lin, S. von Specht, K.-F. Ma, M. Ohrnberger, and F. Cotton, "Analysis of saturation effects of distributed acoustic sensing and detection on signal clipping for strong motions," *Geophys. J. Int.*, vol. 241, no. 2, pp. 971–985, Mar. 2025.

[43] J.-T. Li et al., "Coherently parallel fiber-optic distributed acoustic sensing using dual Kerr soliton microcombs," *Sci. Adv.*, vol. 10, no. 3, Jan. 2024.

[44] Y. Funabiki and M. Miyazawa, "Estimating focal mechanism of small earthquakes using S/P amplitude ratios of distributed acoustic sensing records," *Geophys. Res. Lett.*, vol. 52, no. 9, May 2025, Art. no. e2024GL113963, doi: 10.1029/2024GL113963.

[45] O. H. Waagaard et al., "Real-time low noise distributed acoustic sensing in 171 km low loss fiber," *Opt. Continuum*, vol. 4, no. 2, pp. 688–701, Feb. 2021.

[46] Z. Xiao, J. Chen, Y. Deng, Q. Liu, X. Fan, and Z. He, "Signal-and-kernel phase noise compensation method for distributed acoustic sensors," *J. Lightw. Technol.*, vol. 42, no. 18, pp. 6466–6475, Sep. 2024.

[47] D. Chen, Q. Liu, and Z. He, "Distributed fiber-optic acoustic sensor with sub-nano strain resolution based on time-gated digital OFDR," in *Proc. Asia Commun. Photon. Conf. (ACP)*, Nov. 2017, pp. 1–3.

[48] S. M. Ouellet et al., "Previously hidden landslide processes revealed using distributed acoustic sensing with nanostrain-rate sensitivity," *Nature Commun.*, vol. 15, no. 1, Jul. 2024.

[49] M.-K. Benabid, P. Baumgartner, G. Jin, and Y. Fan, "Leakage detection using distributed acoustic sensing in gas pipelines," *Sensors*, vol. 25, no. 16, p. 4937, Aug. 2025, Art. no. 4937.

[50] Z. Jin, J. Chen, Y. Chang, Q. Liu, and Z. He, "Silicon photonic integrated interrogator for fiber-optic distributed acoustic sensing," *Photon. Res.*, vol. 12, no. 3, p. 465, Mar. 2024.

Guanfeng Chen was born in Guangdong, China, in 1999. He received the B.Eng. degree in measurement and control technology and instrument from Shenzhen University, Shenzhen, China, in 2022, where he is currently pursuing the Ph.D. degree in optical engineering.

His main research interests include distributed optical fiber sensing and signal processing based on FPGAs.

Bin Du was born in Henan, China, in 1992. He received the B.S. degree in flight vehicle propulsion engineering from the School of Astronautics, Beihang University, Beijing, China, in 2016, and the Ph.D. degree in optical engineering from Shenzhen University, Shenzhen, China, in 2021.

From 2021 to 2023, he was a Post-Doctoral Researcher with Guangdong and Hong Kong Joint Research Centre for Optical Fiber Sensors, Shenzhen University. Since 2023, he has been an Associate Researcher with Shenzhen University. His current research interests include distributed optical fiber sensing technology, vibration sensors, and gas sensors.

Baijie Xu was born in Guangdong, China, in 1996. He received the B.S. degree from the College of Physics and Optoelectronic Engineering, Shenzhen University, Shenzhen, China, in 2019, and the Ph.D. degree in optical engineering from Shenzhen University in 2024.

He is currently working as a Post-Doctoral Researcher at Guangdong and Hong Kong Joint Research Centre for Optical Fiber Sensors, Shenzhen University. His current research interests include distributed high-temperature sensing technology and weak fiber Bragg grating arrays.

Huajian Zhong was born in Jiangxi, China, in 1998. He received the bachelor's degree from Changchun University of Science and Technology, Changchun, China, in 2020, and the Ph.D. degree in optical engineering from Shenzhen University, Shenzhen, China, in 2025.

His research interests focus on distributed optical fiber sensing.

Wenzhao Yang was born in Hubei, China, in 2000. He received the bachelor's degree in measurement and control technology and instrumentation from Hubei University of Technology, Wuhan, China, in 2022. He is currently pursuing the master's degree in optoelectronic information engineering with Shenzhen University, Shenzhen, China.

His primary research interests include FPGA implementation of distributed optical fiber sensing and related hardware designs.

Cailing Fu was born in Hubei, China, in 1989. She received the M.S. degree in optical engineering from Wuhan Institute of Technology, Wuhan, China, in 2015, and the Ph.D. degree in optical engineering from Shenzhen University, Shenzhen, China, in 2018.

From 2018 to 2020, she was with the Information and Communication Engineering, Shenzhen University, as a Post-Doctoral Research Fellow. Since June 2020, she has been at Shenzhen University as an Assistant Professor. She has authored or co-authored more than 50 journal articles and conference papers. Her current research interests focus on distributed optical fiber sensing technology.

Yiping Wang (Senior Member, IEEE) was born in Chongqing, China, in 1971. He received the B.Eng. degree in precision instrument engineering from Xi'an Institute of Technology, Xi'an, China, in 1995, and the M.S. and Ph.D. degrees in optical engineering from Chongqing University, Chongqing, in 2000 and 2003, respectively.

From 2003 to 2005, he was with Shanghai Jiao Tong University, Shanghai, China, as a Post-Doctoral Fellow. From 2005 to 2007, he was with The Hong Kong Polytechnic University, Hong Kong, as a Post-Doctoral Fellow. From 2007 to 2009, he was with the Institute of Photonic Technology (IPHT), Jena, Germany, as a Humboldt Research Fellow. From 2009 to 2011, he was with the Optoelectronics Research Centre (ORC), University of Southampton, Southampton, U.K., as a Marie Curie Fellow. Since 2012, he has been with Shenzhen University, Shenzhen, China, as a Distinguished Professor. He has authored or co-authored one book, 25 patent applications, and more than 420 journal articles and conference papers. His current research interests focus on optical fiber sensors, fiber gratings, and photonic crystal fibers.

Prof. Wang is a fellow of the Optical Society of America and the Chinese Optical Society.

Jun He (Member, IEEE) was born in Hubei, China, in 1985. He received the B.Eng. degree in electronic science and technology from Wuhan University, Wuhan, China, in 2006, and the Ph.D. degree in electrical engineering from the Institute of Semiconductors, Chinese Academy of Sciences (CAS), Beijing, China, in 2011.

From 2011 to 2013, he was with Huawei Technologies, Shenzhen, China, as a Research Engineer. From 2013 to 2015, he was with Shenzhen University, Shenzhen, as a Post-Doctoral Research Fellow. From 2015 to 2016, he was with The University of New South Wales Sydney (UNSW), Sydney, NSW, Australia, as a Visiting Fellow. Since 2017, he has been with Shenzhen University as an Assistant Professor/an Associate Professor/Distinguished Professor. He has authored or co-authored eight patent applications and more than 90 journal articles and conference papers. His current research interests focus on optical fiber sensors, fiber Bragg gratings (FBGs), and fiber lasers.

Dr. He is a member of the Optical Society of America.